Electronic properties of transferable atomically thin MoSe 2 /h-BN heterostructures grown on Rh(111)

Ming-Wei Chen, Hokwon Kim, Carlo Bernard, Michele Pizzochero, Javier Zaldívar, Jose Ignacio Pascual, Miguel Ugeda, Oleg Yazyev, Thomas Greber, Jürg Osterwalder, et al.

Electronic Properties of Transferable Atomically Thin MoSe2/h-BN Heterostructures Grown on Rh(111)

Chen, Ming-Wei ; Kim, HoKwon ; Bernard, Carlo ; Pizzochero, Michele ; Zaldívar, Javier ; Pascual, Jose Ignacio ; Ugeda, Miguel M ; Yazyev, Oleg V ; Greber, Thomas ; Osterwalder, Jürg ; Renault, Olivier ; Kis, Andras

DOI: https://doi.org/10.1021/acsnano.8b05628

Electronic Properties of Transferrable Atomically Thin $MoSe_2$/*h*-BN Heterostructures Grown on Rh(111)

Ming-Wei Chen[1,2], HoKwon Kim[1,2], Carlo Bernard[3], Michele Pizzochero[4], Javier Zaldivar Fernandez[5], Jose Ignacio Pascual[5,6], Miguel M. Ugeda[6,7], Oleg V. Yazyev[4], Thomas Greber[3], Jürg Osterwalder[3], Olivier Renault[8,9], Andras Kis[1,2*]

[1]*Electrical Engineering Institute, École Polytechnique Fédérale de Lausanne (EPFL), CH-1015 Lausanne, Switzerland*
[2] *Institute of Materials Science and Engineering, École Polytechnique Fédérale de Lausanne (EPFL), CH-1015 Lausanne, Switzerland*
[3] *Physik-Institut, University of Zurich, Switzerland*
[4] *Institute of Physics, École Polytechnique Fédérale de Lausanne (EPFL), CH-1015 Lausanne, Switzerland*
[5]CIC nanoGUNE, 20018 Donostia-San Sebastian, Spain
[6] *Ikerbasque, Basque Foundation for Science, 48013 Bilbao, Spain.*
[7] *Donostia International Physics Center (DIPC), Manuel Lardizábal 4, 20018 San Sebastián, Spain.*
[8] *Université Grenoble Alpes, F-38000 Grenoble, France*
[9]*CEA, LETI, MINATEC Campus, F-38054 Grenoble, France*
**Correspondence should be addressed to: Andras Kis, andras.kis@epfl.ch*

ABSTRACT

Vertically stacked two-dimensional (2D) heterostructures composed of 2D semiconductors have attracted great attention. Most of these include hexagonal boron nitride (h-BN) as either a substrate, encapsulant or a tunnel barrier. However, reliable synthesis of large-area and epitaxial 2D heterostructures incorporating BN remains challenging. Here, we demonstrate the epitaxial growth of nominal monolayer (ML) $MoSe_2$ on *h*-BN/Rh(111) by molecular beam epitaxy (MBE), where the *h*-BN nanomesh superstructure decouples to form an uncorrelated, atomically smooth interface. The valence band structure of ML $MoSe_2$/*h*-BN/Rh(111) revealed by photoemission electron momentum microscopy (*k*PEEM) shows that the valence band maximum (VBM) located at the *K* point is 1.33 eV below the Fermi level (E_F) while and the energy difference between *K* point and Γ points is determined to be 0.23 eV, demonstrating that the electronic properties such as the direct

bandgap and the effective mass of ML $MoSe_2$ are well preserved in $MoSe_2$/*h*-BN heterostructures.

Keywords: two-dimensional materials, two-dimensional semiconductors, $MoSe_2$, epitaxial growth, *h*-BN substrates

The distinct electronic[1] and optical properties[2,3] make atomically thin two-dimensional materials and transition metal dichalcogenides[4,5] attractive for fundamental research and practical applications. The lack of dangling bonds at their surface makes integration into van der Waals (vdW) heterostructures[6] possible, further extending their reach.

Most of the vdW heterostructures being studied today incorporate hexagonal boron nitride (h-BN) as a substrate[7,8] and encapsulation layer, where the atomically flat surface of h-BN crystals and the low defect density allow accessing the intrinsic properties of 2D materials. Moreover, the wide bandgap of *h*-BN in the UV range makes it promising as a tunnel barrier, while its dielectric properties also allow it to sustain high electric fields before breakdown.[9] However, the reliable preparation of large-area heterostructures remains challenging. The common approach consists of preparing them by mechanical exfoliation and transfer processes, which can introduce residues and contaminants at the interface while the process itself is not scalable.

Chemical vapor deposition has been proposed for growing various 2D materials with good quality, but the use of various precursors for different material systems may increase complexity.[10–13] On the other hand, molecular beam epitaxy (MBE) can provide a promising alternative route and exhibits several potential advantages including the use of the ultra-high vacuum (UHV) environment, high-purity sources and the capability for *in-situ* growth monitoring using reflection-high-energy-electron-diffraction (RHEED). The concept of vdW epitaxy was first proposed by Koma *et al.* in the 1990s, and a wide variety of 2D materials have been studied since then.[6,14–17] However, the MBE-growth of 2D vdW heterostructures

such as $MoSe_2$/*h*-BN[15] needs further study and methods for transferring the resulting heterostack from the metallic substrate also need to be developed.

Here, both the h-BN substrate and the two-dimensional semiconductor $MoSe_2$ are synthesized using scalable methods. We benefit from the previous development of the synthesis of large-scale ML *h*-BN nanomesh on Rh(111),[18–20] and demonstrate the growth of atomically thin $MoSe_2$ on ML *h*-BN/Rh(111) substrates by MBE. There were no intermediate chemical states detected in x-ray photoelectron spectroscopy (XPS) resulting from hybridization. Surprisingly, the 3D nanomesh morphology of BN disappears during $MoSe_2$ growth resulting in an atomically flat surface over the length of the substrate with each layer preserving its lattice constant, in contrast with a previous work on $MoSe_2$/h-BN/Ru(0001) systems (ref [15]). We have also succeeded in transferring the resulting stacks onto insulating substrates. The ML $MoSe_2$/*h*-BN heterostructure after transfer shows photoluminescence (PL) with the main peak at 1.57 eV at room temperature. We further reveal the electronic properties of ML $MoSe_2$/*h*-BN heterostructures by photoemission electron momentum microscopy (*k*PEEM) and perform density functional theory (DFT) calculations to understand the observed effects.

RESULTS

The growth of atomically thin $MoSe_2$/*h*-BN heterostructures

Wafer-scale monolayer (ML) *h*-BN was grown on Rh(111), featuring a nanomesh structure that has been grown using chemical vapor deposition (CVD) in a UHV environment.[18,19] The *h*-BN/Rh(111) wafer was cut into 1 × 1 cm^2 pieces and transferred into a separate MBE system. The growth of $MoSe_2$ was monitored *in-situ* using RHEED. At the growth start, the streaks from epitaxial *h*-BN/Rh(111) were observed along two different azimuths, [10-10] and [11-20], respectively, Figure 1a and b. Satellite patterns representing the nanomesh structures of *h*-BN/Rh(111) can be observed on top of the (00) specular streak. During growth, $MoSe_2$ streaks emerge and remain unchanged until the end of the growth. We estimate that the

growth time for a complete monolayer is ~ 30 min. At this point, we can observe both streaks from the substrate and $MoSe_2$ along the [11-20] azimuth. The streak spacing indicates that the as-grown $MoSe_2$ film retains the crystal lattice registry without showing detectable strain from the substrate, as expected from vdW epitaxy. This finding is also consistent with results obtained from scanning tunneling microscopy (STM), showing that the as-grown epitaxial $MoSe_2$ films were modulated by the underlying *h*-BN while the lattice constants for each layer were preserved (Supplementary section 1). On the other hand, we noticed that in addition to the main $MoSe_2$ streaks shown along the [10-10] azimuth, additional faint streaks also appeared between the main streaks. These could be attributed to the misoriented $MoSe_2$ domains.

We have further examined pristine *h*-BN and as-grown heterostructures using low-energy electron diffraction (LEED). We can clearly observe a transition from the six-fold superstructure spots related to the *h*-BN/Rh(111) nanomesh, to six-fold smeared spots (Figure 1c). An aligned six-fold pattern with a larger lattice constant has also appeared, corresponding to the formation of epitaxial $MoSe_2$, while the ring-pattern indicates the presence of misoriented domains, in line with RHEED observations. From the LEED intensity distribution analysis, the fraction of aligned $MoSe_2$ can be estimated to be over 42 % (Supplementary section 2). Both $MoSe_2$ and *h*-BN have preserved their pristine lattices although the lattice mismatch is as large as ~ 32 % considering epitaxy in the (111) planes.

Spectroscopic analysis of $MoSe_2$/*h*-BN heterostructure

The XPS survey of as-grown $MoSe_2$/*h*-BN/Rh(111) is shown in Figure 2a. The spectrum exhibits a rich feature from both the Rh substrate and the $MoSe_2$/*h*-BN heterostructure. The Mo $3d_{3/2}$ and Se $3d_{3/2}$ core-level spectra shown in Figure 2b and c respectively, exhibit characteristic binding energies of 233.1 eV and 55.7 eV and the intensity ratio is consistent with stoichiometric $MoSe_2$.[14,21] In the Mo 3d core level region, the Se 3s core level peak at 231.7 eV overlaps with the Mo 3d peaks, making precise quantification a challenge.

Nevertheless, the two featured peak positions related to Mo $3d_{3/2,}$ and Mo $3d_{5/2}$ can be easily distinguished, with very little or no trace of oxidation on the high binding energy side.[14] In the Se 3d core level, the binding energy splitting due to spin-orbit coupling can also be deconvoluted, as shown in fits on Figure 2c. The results imply that only Mo-Se covalent bonding exists without a detectable trace of intermediate compounds or oxidation at the interface. Although the signals were mainly from the top layer of $MoSe_2$ and the thicker substrate, we have still observed weak signals corresponding to B 1s and N 1s levels located at binding energies of 190.5 eV and 398.0 eV, respectively. In another sample with the growth time of 60 min, we estimated the stoichiometry by integrating the peak area and found that the $MoSe_2$ film was Se-deficient, with a thickness corresponding to a nominal bilayer, which is consistent with the estimation from RHEED pattern transition (Supplementary section 3).

Photoluminescence (PL) spectroscopy was first performed on as-grown heterostructures at room temperature. No detectable PL signal was seen due to the quenching effect from the metal substrate.[14,15,22] We have therefore adapted an electrochemical delamination process to transfer the as-grown heterostructure onto fresh SiO_2/Si chips.[23–28] Raman spectra of as-grown and transferred $MoSe_2$/*h*-BN are comparable and show A_{1g} modes of $MoSe_2$ at ~ 240 cm^{-1} (Supplementary Note 4). The PL spectrum acquired from the transferred ML $MoSe_2$/*h*-BN heterostructure at room temperature is shown in Figure 2f. The asymmetric spectrum is deconvoluted into two parts. The sharp main peak is located at 792 nm (~ 1.57 eV) with a linewidth of 50 meV, while a broad sideband is found at 816 nm (~ 1.52 eV). The sideband on the low-energy side can be attributed to emission from defect-bound excitons,[29] and possibly originates from the local inhomogeneity of the nominal ML which can broaden the main peak on the low-energy side.[30] On the other hand, the sharp main peak at 1.57 eV at RT is consistent with reported values for ML $MoSe_2$,[29–32] indicating that the PL of transferred ML $MoSe_2$ is not affected by the underlying *h*-BN, as expected, and that it can be quenched by the Rh substrate.

Considering that the emission from trions is supposed to disappear at RT due to thermal fluctuations, the emission should be mainly from the neutral excitons.[32] These results demonstrate the good optical properties of the ML $MoSe_2$/*h*-BN heterostructure.

Photoemission electron momentum microscopy of the ML $MoSe_2$/*h*-BN heterostructure

We have performed *k*PEEM to further investigate the electronic properties of as-grown ML $MoSe_2$/*h*-BN heterostructures. Unlike conventional angle-resolved photoelectron spectroscopy (ARPES) which requires a pre-defined high-symmetry direction and is usually time-consuming due to the sequential acquisition of the *k*-space photoemission signal by sample rotation, *k*PEEM uses parallel angular detection at a given photoelectron energy in the valence band by spectroscopic imaging of the back focal plane of the PEEM. Therefore, the entire reciprocal space is sampled, which makes *k*PEEM an ideal tool for directly assessing the electronic properties of 2D materials.[33,34] The three-dimensional imaging can not only provide the band structures along high symmetry points, but it can also give insights into the film quality and band distortion due to interaction with the substrate.[34,35] Here, *k*PEEM was performed with *off*-normal vacuum ultraviolet (VUV) excitation (He I, $h\nu$ = 21.2 eV), providing an enhanced transition probability at the Γ point,[33,34] thereby facilitating the determination of the VBM.[36]

Representative images of the *k*PEEM spectroscopic image series of the heterostructure are shown in Figure 3. The signal originates from a selected area in real space defined by a field aperture of ~ 20 μm diameter, containing mostly monolayer crystals with a fraction of bilayer areas, corresponding to a diameter of ~ 2 $Å^{-1}$ in reciprocal space, thereby sampling the whole first surface Brillouin zone. In the set of *k*PEEM images, the six-fold symmetry of the bands is clearly revealed, indicating the preferred epitaxial directions of $MoSe_2$. In the image at an energy of 4.10 eV in Figure 3, the first surface Brillouin zone and the characteristic high-symmetry points Γ, *K* and *M* are depicted. We note that the bright spot at the Γ point at the

binding energy of 3.1 eV is related to the underlying *h*-BN, which will be discussed later. In the image stack, we can then perform a cut along the high-symmetry direction Γ to *K* in the binding energy range down to 9.2 eV with respect to $E_F = 0$ eV, allowing us to obtain the full valence band structures of $MoSe_2$/*h*-BN.

DISCUSSION

Electronic properties of the $MoSe_2$/*h*-BN heterostructure

To gain an insight into the valence band structure of $MoSe_2$/*h*-BN, we have first calculated the band structure of freestanding ML $MoSe_2$ by DFT (Figure 4a). Except for the doublet splitting of the valence band induced by spin-orbit coupling, the most significant feature of ML $MoSe_2$ that emerges is the direct bandgap where the VBM is at the *K* point while the Γ point is located 0.23 eV below the VBM. The full valence band structure of nominal ML $MoSe_2$/*h*-BN/Rh(111) along Γ to *K,* derived from the *k*PEEM image series, is shown in Figure 4b. We have further calculated the second derivative of the *k*PEEM images to enhance the contrast and visibility, especially in the upper valence band region (Figure 4c). In the $MoSe_2$/*h*-BN heterostructure, the *h*-BN bands co-exist with $MoSe_2$ bands. The σ-band of *h*-BN originating at a binding energy of 4.0 eV at the Γ point can be identified in Figure 4b and Figure 4c, as the calculated $MoSe_2$ bands in Figure 4a indicate the absence of band features from $MoSe_2$ there. The result is in line with the *k*PEEM image at an energy of 4.1 eV shown in Figure 3. The π-band of *h*-BN, which is expected to disperse from the energy of 8.4 eV at Γ point and up to the energy of 2.4 eV at *K* point, is hardly distinguishable as it is masked by the $MoSe_2$ band structure. In the submonolayer $MoSe_2$/*h*-BN sample, however, the band structure of *h*-BN is much more clearly resolved (Supplementary section 5). This observation of a close-to-ideal *h*-BN band structure is in contrast with the electronic band structure of the h-BN nanomesh on Rh or Ru where split bands can be observed because of the differences in the

interfacial distances between the "pore" and "wire" regions of the nanomesh.[37] Overall, the valence band structure of $MoSe_2$/*h*-BN resembles those of the free-standing counterpart, without any evidence of interlayer hybridization.

We now focus on the upper valence band dispersions of the $MoSe_2$/*h*-BN heterostructure in the momentum space along the Γ to *K* direction. First, we do not observe the spin-splitting but a broad band at the *K* point, likely due to the limited energy resolution (100 meV) provided by the microscope settings used in the experiment, as well as the contribution from the misoriented domains. The *K* point at a binding energy of 1.33 eV below E_F indicates that the as-grown $MoSe_2$ is unintentionally *n*-doped, as observed for a majority of reported $MoSe_2$ atomically thin films.

On the other hand, only one band at an energy of ~1.56 eV at the Γ point is observed, thus indicating that the signal is mainly from the top ML $MoSe_2$ and that the band features of *h*-BN are absent in the upper valence band structure. Additionally, we compare the band maximum at Γ and *K* points, respectively, and observe that the VBM located at the *K* point is higher than the Γ point by 0.23 eV (Supplementary section 6). While this value matches our PBE-DFT calculations for free-standing $MoSe_2$ within the range of error, it is lower than the previously reported value of 0.38 eV for ML $MoSe_2$ grown on bilayer graphene on SiC.[31] This could be due to the use of different substrates and a lower measurement resolution in our case.

The direct bandgap feature of ML $MoSe_2$ is thus preserved in the heterostructure, and the valence band structure is similar to the calculations for free-standing ML $MoSe_2$. The close examination of the experimental and theoretical band structures reveal the presence of a small band compression, often associated with the presence of a substrate.[38,34,35] Similarly, the band dispersions along Γ to *M* are also plotted, and the band structures are in line with the theoretical calculations, with the exception of an energy upshift near the *M* point (Supplementary section 7). Although the differences are small in our case, this is possibly due to screening by the

substrate and charge redistribution at the interface caused by the metallic Rh substrate below the BN monolayer as well as the unintentional *n*-doping of $MoSe_2$. Additionally, a contribution from the misoriented domains and grain boundaries may also be present distorting the apparent band-structure and work function.

To further support our argument that no new hybridization of bands takes place in $MoSe_2$/*h*-BN heterostructures, we have additionally performed vdW-DFT calculations.[39,40] The vertical heterostructure was modeled considering a (3 × 3) $MoSe_2$ supercell ($a_{MoSe2} \approx 3.3$ Å) on top of a (4 × 4) *h*-BN supercell ($a_{h\text{-}BN} \approx 2.5$ Å), as sketched in Figure 5a. Our simulations suggest that ML $MoSe_2$ is located ~3.6 Å above the *h*-BN plane, with an interlayer interaction of ~90 meV per f.u. and an adhesive energy of ~9 meV/Å^2 per f.u. (Supplementary Table 1). This latter value is below the typical adhesive energy of van der Waals-layered materials, estimated to be in the range of 13 - 21 meV/Å^2, thereby indicating a very weak coupling between the two layers in the heterostructure.[41] Figure 5b shows the charge transfer that takes place in the heterostructure: negative charge density distributes on both h-BN and $MoSe_2$ MLs, while positive charge accumulates in the interlayer region. Furthermore, the results of our vdW-DFT calculations presented in Figure 5c suggest that in the heterostructure, the *h*-BN electronic states exist only below the energy of 0.7 eV below the VBM as indicated by the dashed line. Therefore, $MoSe_2$ band edges are retained upon heterostructure formation, and the ML feature such as the direct bandgap is thus preserved (Supplementary Figures 8 and 9).

It is not clear why the nanomesh structure disappears with the deposition of $MoSe_2$, resulting in an atomically flat interface. The decoupling of h-BN from Rh occurs early in the MBE growth process as described in the Supplementary section 5. This was not the case for the $MoSe_2$/h-BN/Ru system deposited by MBE[15] where the nanomesh structure is unchanged even after the growth, and the electronic property of $MoSe_2$ is modulated by the morphological

variations due to the strong interaction with Ru. A similar disappearance of the nanomesh structure as in our case was observed for the graphene/*h*-BN/Rh(111) system where the decoupling was assisted by the interfacial carbon formation between BN and Rh during the CVD growth of graphene. Here, we saw no evidence for the existence of the interfacial layer and further investigation of the exact growth mechanism is required. Nevertheless, this route can be highly advantageous for utilizing technologically attractive qualities of the atomically flat, freestanding layers of $MoSe_2$ and other TMDCs.

CONCLUSION

In conclusion, we demonstrate the growth of $MoSe_2$/*h*-BN heterostructures on Rh(111) with preferential lattice alignment *via* vdW epitaxy. The electronic properties of nominal ML $MoSe_2$/*h*-BN were directly revealed by *k*PEEM, showing the direct bandgap whith the VBM located at the *K* point and 0.23 eV above *Γ* point. Additionally, the as-grown $MoSe_2$ was found to be virtually free-standing as the nanomesh h-BN structure becomes atomically flat during the growth. Photoluminescence from monolayer $MoSe_2$/*h*-BN can be detected after delaminating the heterostructure from the Rh substrate, and the electronic structures of the as-grown $MoSe_2$ remain preserved in the presence of the underlying *h*-BN, as confirmed by first-principles calculations. This work provides deep insights into the growth of TMDCs on h-BN with highly attractive optoelectronic properties of pristine monolayer semiconductors.

METHODS

Material growth

The growth was carried out in an Omicron MBE with ~ 10^{-10} mbar base pressure. Cleaved 1 × 1 cm^2 *h*-BN/Rh(111)/YSZ/Si(111) substrates were outgassed at up to 500 ºC for 12 hrs prior to growth. The growth was conducted at 350 ºC with a fixed Se/Mo ratio ~ 40 and a Mo

deposition rate of ~ 0.1 Å/min; the temperature was monitored using a pyrometer, and the flux for each cell was calibrated using a quartz crystal microbalance. After growth, the sample was post-annealed *in-situ* at the same temperature with Se flux at 400 ºC for 20 mins. A RHEED camera (STAIB Co.) was used to monitor the growth *in-situ*. The LEED and photoelectron diffraction experiments were performed in the surface science laboratory at the University of Zurich.[42]

XPS and Raman spectrum and PL characterizations

The XPS spectra were *ex-situ* obtained in a commercial ULVC-PHI Versa Probe II system with a laboratory Al Kα X-ray source (hν = 1486.6 eV), and the C1s core level peak at 284.8 eV was used as the reference for determining the binding energies. Peak identification and fitting was processed in PHI's MultiPak processing software. The PL and Raman were measured in using a 532-nm-wavelength laser in a Renishaw Raman confocal microscope.

Photoemission electron momentum microscopy (*k*PEEM)

The experimental details of the instrument and *k*PEEM measurements can be found in previous reports.[33,34] In short, a *NanoESCA* MkI spectro-microscope (ScientaOmicron) equipped with a helium cold cathode lamp (*hv* = 21.2 eV) was used for room-temperature *k*PEEM analysis in UHV conditions (2×10^{-10} mbar). The analyzer pass energy of 100 and 50 eV with an entrance slit size of 1 mm provided an energy resolution of 200 meV and 100 meV, respectively.

First-principles simulations

Our calculations were performed within the DFT framework, as implemented in the SIESTA code. In order to describe the exchange and correlations effects, we used the generalized gradient approximations of Perdew, Burke and Ernzerhof (PBE) for free-standing $MoSe_2$ and several vdW density functionals (BH, C09, DRSLL, KBM, LMKLL) for the

$MoSe_2$/*h*-BN heterostructure. Spin-orbit coupling was included only in the calculation of the band structure of free-standing $MoSe_2$. Core electrons were replaced with relativistic, Troullier-Martins pseudopotentials whereas valence electrons were described with a Tζ *plus* double polarization (TZDP) basis set in conjunction with a mesh-cutoff of 450 Ry. The basis set superposition error was systematically corrected following the counterpoise scheme. The Brillouin zone was sampled with the equivalent of 30 × 30 × 1 k-points per $MoSe_2$ unit cell during geometry relaxation runs and 120 × 120 × 1 k-points for the calculations of the electronic density of states. Tolerance on forces during relaxations was set to 15 meV/Å while lattice constants were set to be equal to that of the ML $MoSe_2$ and a vacuum region 29 Å thick was included to separate periodic replicas.

ACKNOWLEDGEMENTS

We thank M. Cantoni and D. Alexander (CIME) for FIB operation and for support with electron microscopy. We thank P. Mettraux for XPS setup and experiments. The momentum microscopy was performed in the Platform for NanoCharacterization (PFNC) of MINATEC Campus within CEA-Grenoble research center. The access was provided by the NFFA-Europe Infrastructure (proposal ID 121) under Horizon 2020 EU Funding Program. We thank N. Gambacorti for coordinating the access to the NFFA-EU program.

This work was financially supported by the European Research Council (grant no. 240076) and has received funding from the European Union's Horizon 2020 research and innovation programme under grant agreement No 696656 and 785219 (Graphene Flagship Core 1 and Core 2). M. P. acknowledges support by the Swiss National Science Foundation (grant No. 200021-162612). First-principles calculations were performed at the Swiss National Supercomputing Centre (CSCS) under the project s832.

REFERENCES

(1) Radisavljevic, B.; Radenovic, A.; Brivio, J.; Giacometti, V.; Kis, A. Single-Layer MoS_2 Transistors. *Nat. Nanotechnol.* **2011**, *6*, 147–150.

(2) Splendiani, A.; Sun, L.; Zhang, Y.; Li, T.; Kim, J.; Chim, C.-Y.; Galli, G.; Wang, F. Emerging Photoluminescence in Monolayer MoS_2. *Nano Lett.* **2010**, *10*, 1271–1275.

(3) Mak, K. F.; Lee, C.; Hone, J.; Shan, J.; Heinz, T. F. Atomically Thin MoS_2: A New Direct-Gap Semiconductor. *Phys. Rev. Lett.* **2010**, *105*, 136805.

(4) Wang, Q. H.; Kalantar-Zadeh, K.; Kis, A.; Coleman, J. N.; Strano, M. S. Electronics and Optoelectronics of Two-Dimensional Transition Metal Dichalcogenides. *Nat. Nanotechnol.* **2012**, *7*, 699–712.

(5) Manzeli, S.; Ovchinnikov, D.; Pasquier, D.; Yazyev, O. V.; Kis, A. 2D Transition Metal Dichalcogenides. *Nat. Rev. Mater.* **2017**, *2*, 1733.

(6) Koma, A. Van Der Waals Epitaxy - a New Epitaxial-Growth Method for a Highly Lattice-Mismatched System. *Thin Solid Films* **1992**, *216*, 72–76.

(7) Dean, C. R.; Young, A. F.; Meric, I.; Lee, C.; Wang, L.; Sorgenfrei, S.; Watanabe, K.; Taniguchi, T.; Kim, P.; Shepard, K. L.; Hone, J. Boron Nitride Substrates for High-Quality Graphene Electronics. *Nat. Nanotechnol.* **2010**, *5*, 722–726.

(8) Yang, W.; Chen, G.; Shi, Z.; Liu, C.-C.; Zhang, L.; Xie, G.; Cheng, M.; Wang, D.; Yang, R.; Shi, D.; Watanabe, K.; Taniguchi, T.; Yao, Y.; Zhang, Y.; Zhang, G. Epitaxial Growth of Single-Domain Graphene on Hexagonal Boron Nitride. *Nat. Mater.* **2013**, *12*, 792–797.

(9) Britnell, L.; Gorbachev, R. V.; Jalil, R.; Belle, B. D.; Schedin, F.; Katsnelson, M. I.; Eaves, L.; Morozov, S. V.; Mayorov, A. S.; Peres, N. M. R.; Castro Neto, A. H.; Leist, J.; Geim, A. K.; Ponomarenko, L. A.; Novoselov, K. S. Electron Tunneling through Ultrathin Boron Nitride Crystalline Barriers. *Nano Lett.* **2012**, *12*, 1707–1710.

(10) Chhowalla, M.; Shin, H. S.; Eda, G.; Li, L.-J.; Loh, K. P.; Zhang, H. The Chemistry of Two-Dimensional Layered Transition Metal Dichalcogenide Nanosheets. *Nat. Chem.* **2013**, *5*, 263–275.

(11) Dumcenco, D.; Ovchinnikov, D.; Marinov, K.; Lazić, P.; Gibertini, M.; Marzari, N.; Sanchez, O. L.; Kung, Y.-C.; Krasnozhon, D.; Chen, M.-W.; Bertolazzi, S.; Gillet, P.; Fontcuberta i Morral, A.; Radenovic, A.; Kis, A. Large-Area Epitaxial Monolayer MoS_2. *ACS Nano* **2015**, *9*, 4611–4620.

(12) Fu, L.; Sun, Y.; Wu, N.; Mendes, R. G.; Chen, L.; Xu, Z.; Zhang, T.; Rümmeli, M. H.; Rellinghaus, B.; Pohl, D.; Zhuang, L.; Fu, L. Direct Growth of MoS_2/h-BN Heterostructures *via* a Sulfide-Resistant Alloy. *ACS Nano* **2016**.

(13) Wang, S.; Wang, X.; Warner, J. H. All Chemical Vapor Deposition Growth of MoS_2:H-BN Vertical van Der Waals Heterostructures. *ACS Nano* **2015**, *9*, 5246–5254.

(14) Vishwanath, S.; Liu, X.; Rouvimov, S.; Mende, P. C.; Azcatl, A.; McDonnell, S.; Wallace, R. M.; Feenstra, R. M.; Furdyna, J. K.; Jena, D.; Grace Xing, H. Comprehensive Structural and Optical Characterization of MBE Grown $MoSe_2$ on Graphite, CaF_2 and Graphene. *2D Mater.* **2015**, *2*, 024007.

(15) Zhang, Q.; Chen, Y.; Zhang, C.; Pan, C.-R.; Chou, M.-Y.; Zeng, C.; Shih, C.-K. Bandgap Renormalization and Work Function Tuning in $MoSe_2$/HBN/Ru(0001) Heterostructures. *Nat. Commun.* **2016**, *7*, 13843.

(16) Chen, M.-W.; Ovchinnikov, D.; Lazar, S.; Pizzochero, M.; Whitwick, M. B.; Surrente, A.; Baranowski, M.; Sanchez, O. L.; Gillet, P.; Plochocka, P.; Yazyev, O. V.; Kis, A. Highly Oriented Atomically Thin Ambipolar $MoSe_2$ Grown by Molecular Beam Epitaxy. *ACS Nano* **2017**.

(17) Chen, M.-W.; Kim, H.; Ovchinnikov, D.; Kuc, A.; Heine, T.; Renault, O.; Kis, A. Large-Grain MBE-Grown GaSe on GaAs with a Mexican Hat-like Valence Band Dispersion. *Npj 2D Mater. Appl.* **2018**, *2*.
(18) Corso, M.; Auwärter, W.; Muntwiler, M.; Tamai, A.; Greber, T.; Osterwalder, J. Boron Nitride Nanomesh. *Science* **2004**, *303*, 217–220.
(19) Hemmi, A.; Bernard, C.; Cun, H.; Roth, S.; Klöckner, M.; Kälin, T.; Weinl, M.; Gsell, S.; Schreck, M.; Osterwalder, J.; Greber, T. High Quality Single Atomic Layer Deposition of Hexagonal Boron Nitride on Single Crystalline Rh(111) Four-Inch Wafers. *Rev. Sci. Instrum.* **2014**, *85*, 035101.
(20) Roth, S.; Matsui, F.; Greber, T.; Osterwalder, J. Chemical Vapor Deposition and Characterization of Aligned and Incommensurate Graphene/Hexagonal Boron Nitride Heterostack on Cu(111). *Nano Lett.* **2013**, *13*, 2668–2675.
(21) Xenogiannopoulou, E.; Tsipas, P.; Aretouli, K. E.; Tsoutsou, D.; Giamini, S. A.; Bazioti, C.; Dimitrakopulos, G. P.; Komninou, P.; Brems, S.; Huyghebaert, C.; Radu, I. P.; Dimoulas, A. High-Quality, Large-Area $MoSe_2$ and $MoSe_2/Bi_2Se_3$ Heterostructures on AlN(0001)/Si(111) Substrates by Molecular Beam Epitaxy. *Nanoscale* **2015**, *7*, 7896–7905.
(22) Jiao, L.; Liu, H. J.; Chen, J. L.; Yi, Y.; Chen, W. G.; Cai, Y.; Wang, J. N.; Dai, X. Q.; Wang, N.; Ho, W. K.; Xie, M. H. Molecular-Beam Epitaxy of Monolayer $MoSe_2$: Growth Characteristics and Domain Boundary Formation. *New J. Phys.* **2015**, *17*, 053023.
(23) Wang, Y.; Zheng, Y.; Xu, X.; Dubuisson, E.; Bao, Q.; Lu, J.; Loh, K. P. Electrochemical Delamination of CVD-Grown Graphene Film: Toward the Recyclable Use of Copper Catalyst. *ACS Nano* **2011**, *5*, 9927–9933.
(24) Gao, L.; Ren, W.; Xu, H.; Jin, L.; Wang, Z.; Ma, T.; Ma, L.-P.; Zhang, Z.; Fu, Q.; Peng, L.-M.; Bao, X.; Cheng, H.-M. Repeated Growth and Bubbling Transfer of Graphene with Millimetre-Size Single-Crystal Grains Using Platinum. *Nat. Commun.* **2012**, *3*, 699.
(25) Kim, G.; Jang, A.-R.; Jeong, H. Y.; Lee, Z.; Kang, D. J.; Shin, H. S. Growth of High-Crystalline, Single-Layer Hexagonal Boron Nitride on Recyclable Platinum Foil. *Nano Lett.* **2013**, *13*, 1834–1839.
(26) Wen, Y.; Shang, X.; Dong, J.; Xu, K.; He, J.; Jiang, C. Ultraclean and Large-Area Monolayer Hexagonal Boron Nitride on Cu Foil Using Chemical Vapor Deposition. *Nanotechnology* **2015**, *26*, 275601.
(27) Caneva, S.; Weatherup, R. S.; Bayer, B. C.; Blume, R.; Cabrero-Vilatela, A.; Braeuninger-Weimer, P.; Martin, M.-B.; Wang, R.; Baehtz, C.; Schloegl, R.; Meyer, J. C.; Hofmann, S. Controlling Catalyst Bulk Reservoir Effects for Monolayer Hexagonal Boron Nitride CVD. *Nano Lett.* **2016**, *16*, 1250–1261.
(28) Cun, H.; Hemmi, A.; Miniussi, E.; Bernard, C.; Probst, B.; Liu, K.; Alexander, D. T. L.; Kleibert, A.; Mette, G.; Weinl, M.; Schreck, M.; Osterwalder, J.; Radenovic, A.; Greber, T. Centimeter-Sized Single-Orientation Monolayer Hexagonal Boron Nitride With or Without Nanovoids. *Nano Lett.* **2018**.
(29) Tongay, S.; Suh, J.; Ataca, C.; Fan, W.; Luce, A.; Kang, J. S.; Liu, J.; Ko, C.; Raghunathanan, R.; Zhou, J.; Ogletree, F.; Li, J.; Grossman, J. C.; Wu, J. Defects Activated Photoluminescence in Two-Dimensional Semiconductors: Interplay between Bound, Charged, and Free Excitons. *Sci. Rep.* **2013**, *3*, 2657.
(30) Tonndorf, P.; Schmidt, R.; Böttger, P.; Zhang, X.; Börner, J.; Liebig, A.; Albrecht, M.; Kloc, C.; Gordan, O.; Zahn, D. R. T.; Michaelis de Vasconcellos, S.; Bratschitsch, R. Photoluminescence Emission and Raman Response of Monolayer MoS_2, $MoSe_2$, and WSe_2. *Opt. Express* **2013**, *21*, 4908–4916.

(31) Zhang, Y.; Chang, T.-R.; Zhou, B.; Cui, Y.-T.; Yan, H.; Liu, Z.; Schmitt, F.; Lee, J.; Moore, R.; Chen, Y.; Lin, H.; Jeng, H.-T.; Mo, S.-K.; Hussain, Z.; Bansil, A.; Shen, Z.-X. Direct Observation of the Transition from Indirect to Direct Bandgap in Atomically Thin Epitaxial $MoSe_2$. *Nat. Nanotechnol.* **2014**, *9*, 111–115.

(32) Ross, J. S.; Wu, S.; Yu, H.; Ghimire, N. J.; Jones, A. M.; Aivazian, G.; Yan, J.; Mandrus, D. G.; Xiao, D.; Yao, W.; Xu, X. Electrical Control of Neutral and Charged Excitons in a Monolayer Semiconductor. *Nat. Commun.* **2013**, *4*, 1474.

(33) Frégnaux, M.; Kim, H.; Rouchon, D.; Derycke, V.; Bleuse, J.; Voiry, D.; Chhowalla, M.; Renault, O. Chemistry and Electronics of Single Layer MoS_2 Domains from Photoelectron Spectromicroscopy Using Laboratory Excitation Sources. *Surf. Interface Anal.* **2016**, *48*, 465–469.

(34) Kim, H.; Dumcenco, D.; Frégnaux, M.; Benayad, A.; Chen, M.-W.; Kung, Y.-C.; Kis, A.; Renault, O. Free-Standing Electronic Character of Monolayer MoS_2 in van Der Waals Epitaxy. *Phys. Rev. B* **2016**, *94*, 081401.

(35) Diaz, H. C.; Ma, Y.; Kolekar, S.; Avila, J.; Chen, C.; Asensio, M. C.; Batzill, M. Substrate Dependent Electronic Structure Variations of van Der Waals Heterostructures of $MoSe_2$ or $MoSe_{2(1-x)}Te_{2x}$ Grown by van Der Waals Epitaxy. *2D Mater.* **2017**, *4*, 025094.

(36) Jin, W.; Yeh, P.-C.; Zaki, N.; Zhang, D.; Sadowski, J. T.; Al-Mahboob, A.; van der Zande, A. M.; Chenet, D. A.; Dadap, J. I.; Herman, I. P.; Sutter, P.; Hone, J.; Osgood, R. M. Direct Measurement of the Thickness-Dependent Electronic Band Structure of MoS_2 Using Angle-Resolved Photoemission Spectroscopy. *Phys. Rev. Lett.* **2013**, *111*, 106801.

(37) Roth, S.; Greber, T.; Osterwalder, J. Some Like It Flat: Decoupled h-BN Monolayer Substrates for Aligned Graphene Growth. *ACS Nano* **2016**, *10*, 11187–11195.

(38) Jin, W.; Yeh, P.-C.; Zaki, N.; Chenet, D.; Arefe, G.; Hao, Y.; Sala, A.; Mentes, T. O.; Dadap, J. I.; Locatelli, A.; Hone, J.; Osgood, R. M. Tuning the Electronic Structure of Monolayer Graphene/MoS_2 van Der Waals Heterostructures *via* Interlayer Twist. *Phys. Rev. B* **2015**, *92*, 201409.

(39) Soler, J. M.; Artacho, E.; Gale, J. D.; García, A.; Junquera, J.; Ordejón, P.; Daniel Sánchez-Portal. The SIESTA Method for *Ab Initio* Order- N Materials Simulation. *J. Phys. Condens. Matter* **2002**, *14*, 2745.

(40) Berland, K.; Cooper, V. R.; Lee, K.; Schröder, E.; Thonhauser, T.; Hyldgaard, P.; Lundqvist, B. I. Van Der Waals Forces in Density Functional Theory: A Review of the VdW-DF Method. *Rep. Prog. Phys.* **2015**, *78*, 066501.

(41) Björkman, T.; Gulans, A.; Krasheninnikov, A. V.; Nieminen, R. M. Van Der Waals Bonding in Layered Compounds from Advanced Density-Functional First-Principles Calculations. *Phys. Rev. Lett.* **2012**, *108*, 235502.

(42) A photoelectron spectrometer for k-space mapping above the Fermi level: Review of Scientific Instruments: Vol 68, No 12 http://aip.scitation.org/doi/abs/10.1063/1.1148429 (accessed Aug 18, 2017).

FIGURES

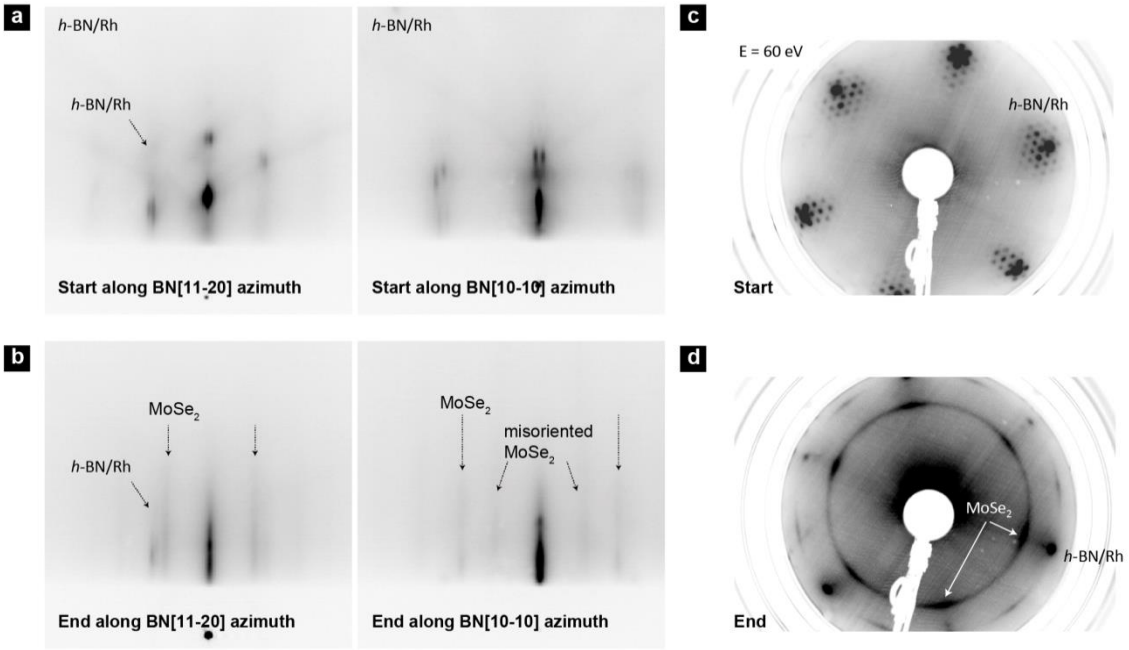

Figure 1. Growth of atomically thin $MoSe_2$/h-BN heterostructures. (a) and (b) *in-situ* RHEED observation during growth along h-BN[11-20] and [10-10] azimuths, respectively. $MoSe_2$ streaks are indicated by black arrows. (c) LEED observation of pristine *h*-BN and the as-grown $MoSe_2$/*h*-BN heterostructure.

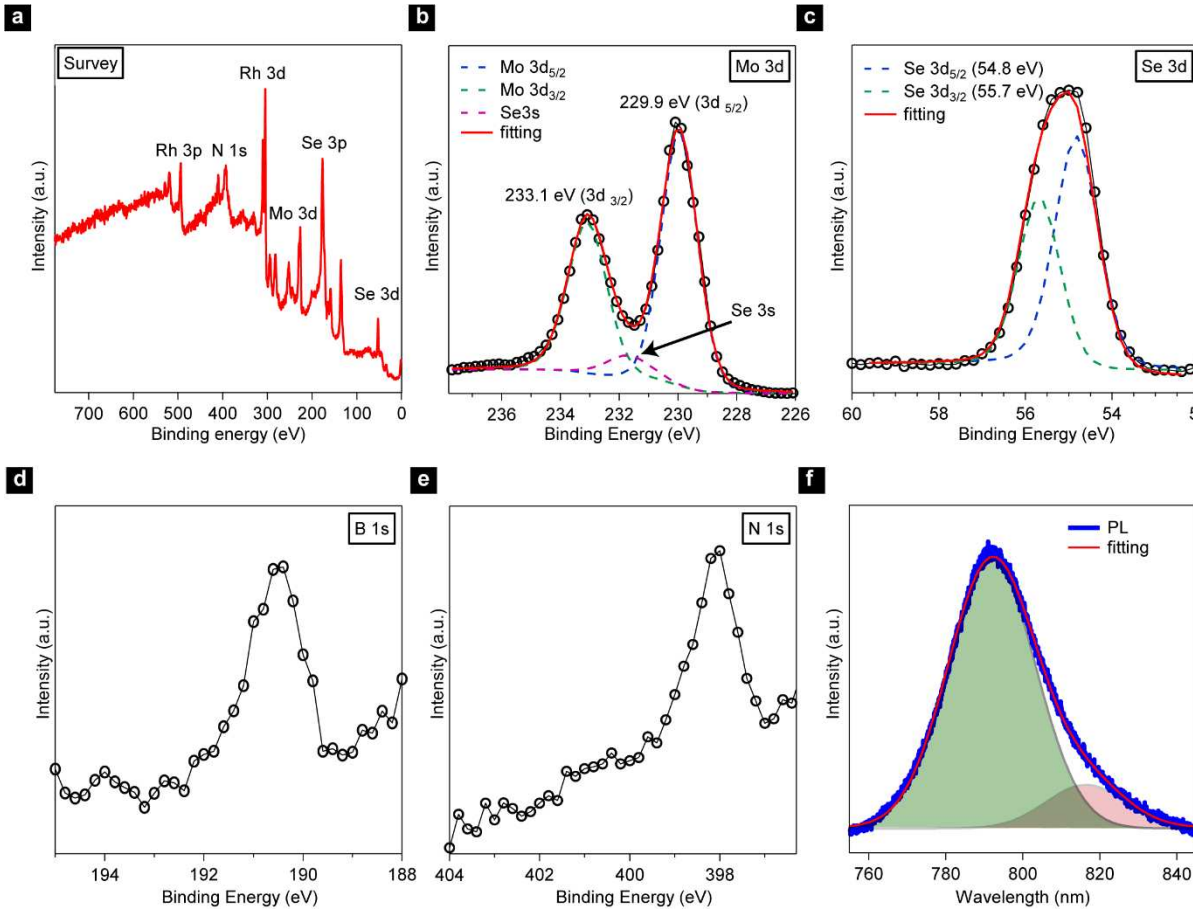

Figure 2. XPS analysis of the $MoSe_2$/*h*-BN heterostructure. (a) Survey spectrum of the heterostructure. Core-level spectra of (b) Mo 3d (c) Se 3d (d) B 1s (e) N 1s. (f) Room-temperature PL of the heterostructure transferred onto SiO_2/Si and the fitting (red line) with the deconvolution into two peaks.

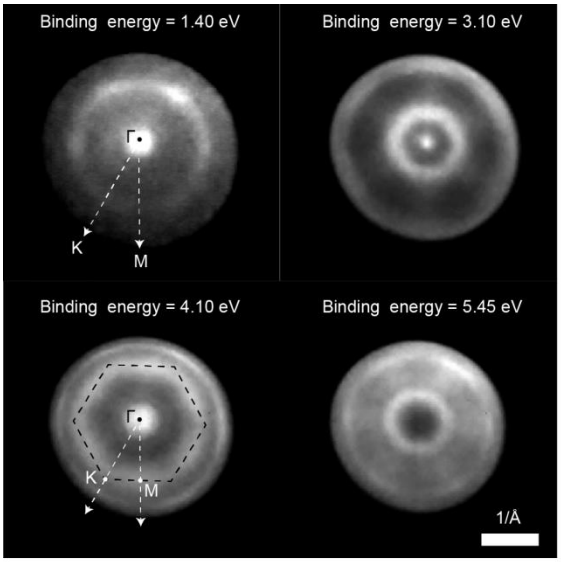

Figure 3. Imaging of heterostructures in *k*-space by *k*PEEM. Images were acquired at different binding energy levels, and the six-fold symmetry is highlighted depicting the 1st surface Brillouin zone. The high symmetry points Γ, K and M of the dominant $MoSe_2$ lattice in *k*-space are shown.

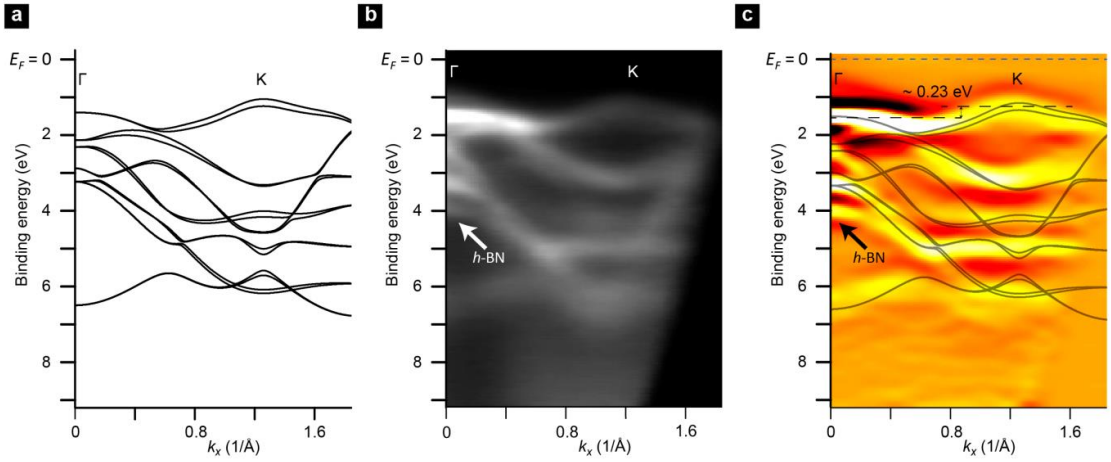

Figure 4. Electronic structures of nominal ML $MoSe_2$/*h*-BN. (a) Calculated band structures of free-standing ML $MoSe_2$. (b) Reslice of *k*-space along the *Γ*-*K* direction and (c) the second-derivative band structure for enhanced contrast. The calculated structures (black lines) are shown in comparison, and the band maximums at *Γ* and *K* with the energy difference are specified. The blue dashed line in (c) refers to E_F = 0 eV.

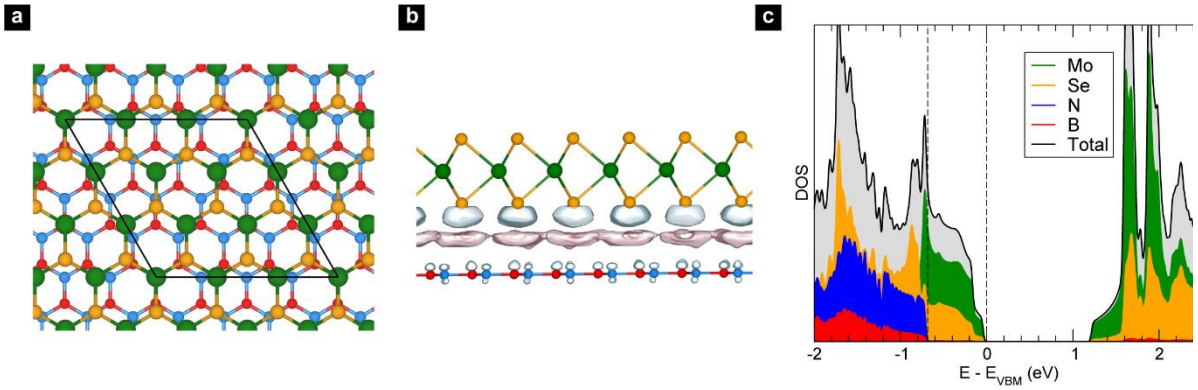

Figure 5. DFT calculations of $MoSe_2$/*h*-BN heterostructure. (a) Top view of the model adopted in our vdW-DFT simulations; green, orange, red and blue balls represent Mo, Se, B and N atoms, respectively (b) Difference in charge density between the heterostructure and isolated $MoSe_2$ and *h*-BN MLs as obtained with the DRSLL functional; grey (pink) clouds indicate negative (positive) charge and isosurfaces were set to 0.003 *e*/Å³ (c) electronic density of states of the $MoSe_2$/*h*-BN heterostructure, as obtained with the DRSLL functional; B and N states are doubled to guide the eye and vertical black dashed lines indicate $MoSe_2$ and *h*-BN valence band edges.

Supplementary Information: Electronic Properties of Transferrable Atomically Thin $MoSe_2$/*h*-BN Heterostructures Grown On Rh(111)

Ming-Wei Chen[1,2], HoKwon Kim[1,2], Carlo Bernard[3], Michele Pizzochero[4], Javier Zaldivar Fernandez[5], Jose Ignacio Pascual[5,6], Miguel M. Ugeda[6,7], Oleg V. Yazyev[4], Thomas Greber[3], Jürg Osterwalder[3], Olivier Renault[8,9], Andras Kis[1,2*]

**Correspondence should be addressed to: Andras Kis, andras.kis@epfl.ch*

1. Lattice modulation of $MoSe_2$/*h*-BN observed by scanning tunneling microscopy

The as-grown ML $MoSe_2$/*h*-BN heterostructure was transferred to a commercial (SPECS GmbH) UHV-LT-STM operated at 1.2 K to be imaged with atomic resolution. In order to prevent the degradation during transport through air to the UHV-STM chamber, a Se capping layer with a thickness of ~ 10 nm was deposited on the sample surface after growth. For the STM experiments, the Se capping layer was removed by annealing the sample at ~ 670 K in UHV for 200 minutes. SI Fig. 1a shows several atomically flat terraces representing the exposed *h*-BN/Rh(111) area from the as-grown heterostructure. The *h*-BN/Rh(111) is visible due to the fact that the growth does not strictly follow the layer-by-layer mode, and the inhomogeneous deposition may also play a role. Therefore, we could both observe the *h*-BN/Rh(111) and as-grown $MoSe_2$ regions in the same sample. Surprisingly, the close-up image of *h*-BN/Rh(111) from the boxed region in SI Fig. 1b reveals a characteristic 1.5 nm x 1.5 nm moiré pattern (outlined with the white diamond) that arises due to the mismatch and relative rotation (8.98° for a 1.5 nm superlattice constant) between the *h*-BN and Rh(111) atomic lattices. The results imply that *h*-BN might be decoupled from the Rh(111) during the growth,[1] and the superlattice no longer resembles the nanomesh structure with ~ 3.2 nm periodicity. We suspect that the decoupling could be from the intercalation either by Mo or Se during growth. This modification of the surface is also evident from the RHEED pattern (Fig. 1) which features satellite spots immediately becomimg fuzzy at the start of the growth with new streaks of $MoSe_2$ appearing later. The *k*PEEM results from another sample with sub-ML $MoSe_2$ can be seen in Supplementary Section 5 and are in line with our speculations since the splitting of σ-band disappears at the early growth phase. SI Fig 1c shows an atomically resolved STM image of the ML $MoSe_2$/*h*-BN heterostructure from the squared box in SI Fig. 1d. The underlying moiré pattern from *h*-BN/Rh(111) (outlined with the white diamond) is also visible. The transparency of as-grown $MoSe_2$ and the preserved moiré pattern support the preferred epitaxy we observed in RHEED and LEED in the main text. The STM image in SI Fig. 1d shows the typical morphology of our sample. The first layer of $MoSe_2$ (dark blue) mostly covers the *h*-BN substrate (black), and it is decorated by small patches of the second $MoSe_2$ layer (light blue). The epitaxial $MoSe_2$ layers show typical mirror twin boundaries commonly found in MBE-grown TMD semiconductors.[2] The apparent height of the ML and the BL with respect to the *h*-BN substrate measured along the red line in SI Fig. 1d is shown in SI Fig. 1e.

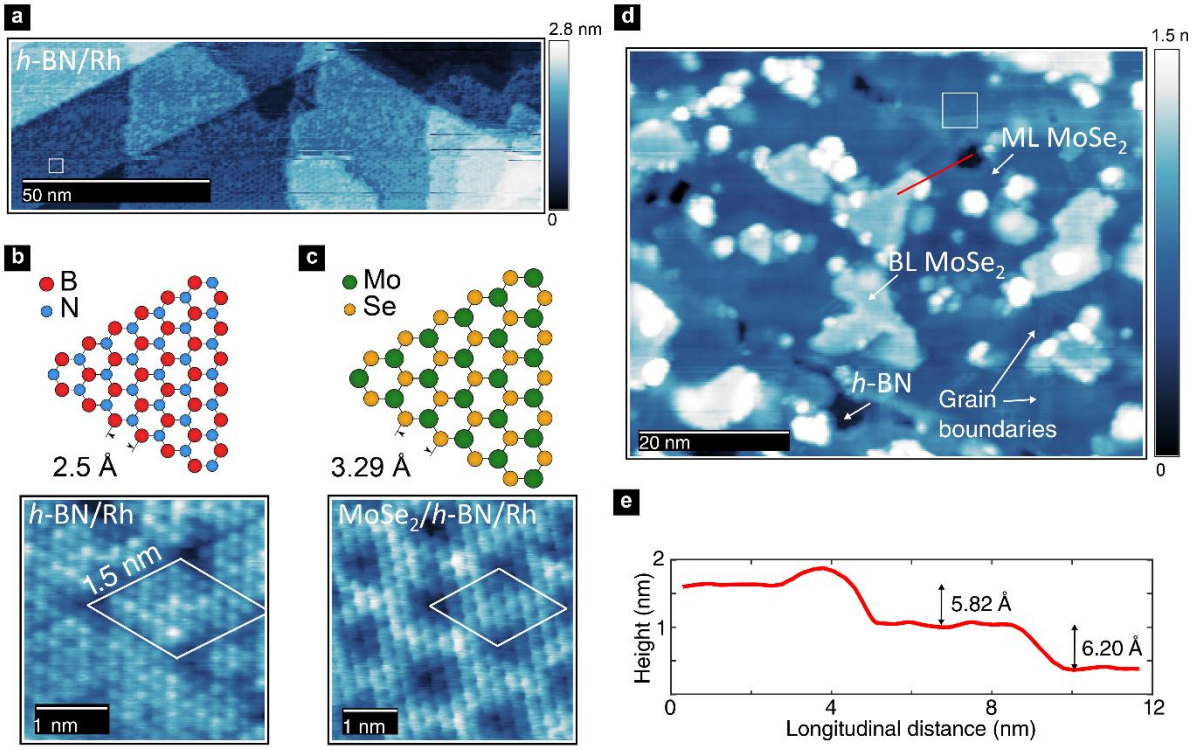

SI Fig. 1. Lattice modulation of as-grown $MoSe_2$/*h*-BN observed by scanning tunneling microscopy. (a) A scan from the exposed *h*-BN/Rh(111) region in the same sample without $MoSe_2$ coverage. (b) Close-up image of *h*-BN/Rh(111) from the boxed region in (a), and the superlattice outlined with the white diamond. (c) Close-up image of ML $MoSe_2$ area. The superlattice from *h*-BN/Rh remains unchanged, indicating the aligned $MoSe_2$. The close-up image is acquired from the image shown in (d). (d) The typical morphology of our sample. (e) Height profile of ML and BL $MoSe_2$ acquired from the cut along the red line in (d).

2. LEED and XPD analysis

The as-grown ML $MoSe_2$/*h*-BN heterostructure was analyzed using LEED at 70 eV (SI Fig. 2a). The red dashed ring represents the as-grown $MoSe_2$, and the signal corresponding to the two blue rings is used for background subtraction. The intensity profile along the azimuthal cut after background subtraction is shown in SI Fig. 2b. The Lorentzian peak-width of the epitaxial $MoSe_2$ (single orientation peaks) is derived from the polar LEED intensity profiles (not shown). After fitting the intensity of these peaks, the intensity residues in between the peaks represent misoriented $MoSe_2$. With this data analysis, 42% of the $MoSe_2$ appears to be epitaxially aligned to the h-BN substrate.

The X-ray photoelectron diffraction (XPD) results of Mo $3d_{5/2}$ and Se $3d_{5/2}$ lines are shown in SI. Fig. 2c. The six-fold symmetry for both patterns can be easily identified, demonstrating crystalline films with a predominant azimuthal orientation. Furthermore, the bright diffraction spot in the center of the diffraction map (along the surface normal) represents forward scattering and indicates a stacking order of Mo (Se) on top of Se (Mo) atom. We thus conclude that this feature stems from the 2H-polytype $MoSe_2$. In the plot of the signal ratio vs. polar angle (SI Fig. 2d), the Se/N signal ratio first decreases with the polar angle and remains constant, indicating the above-mentioned Se forward scattering peak.

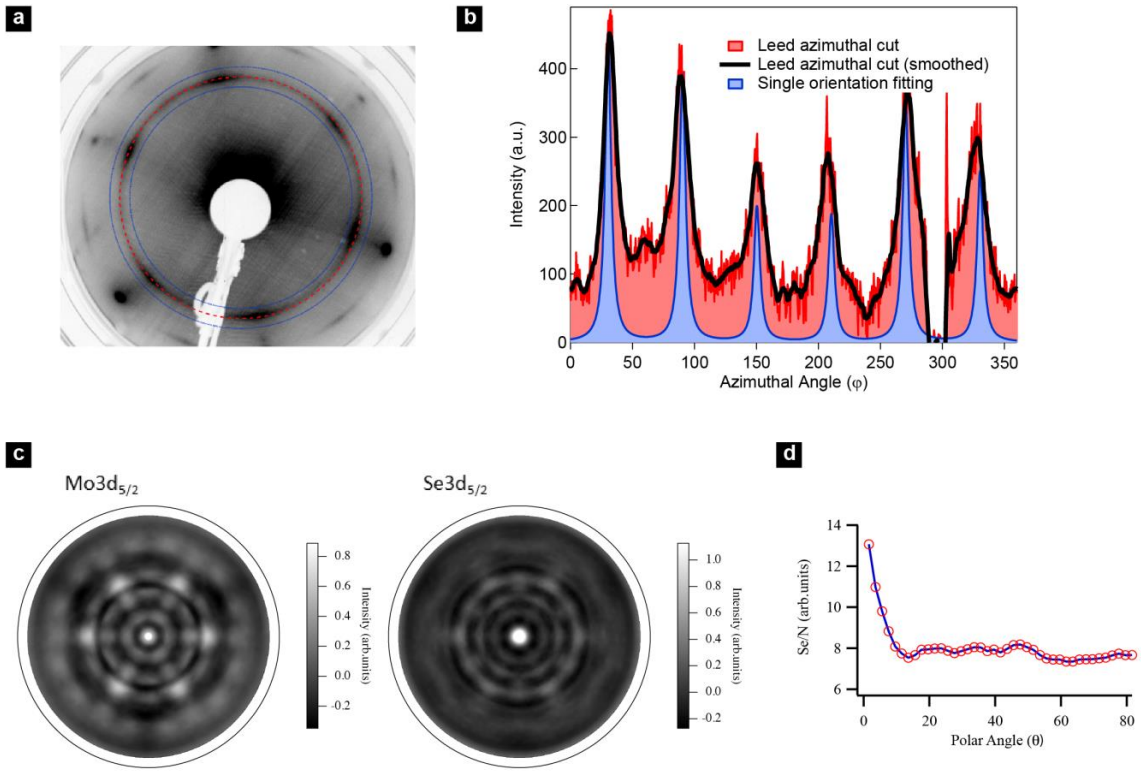

SI Fig. 2. LEED and XPD analysis. (a) LEED image of $MoSe_2$/*h*-BN/Rh(111). (b) Intensity profile of the ring in LEED. (c) XPD of Mo $3d_{5/2}$ and Se $3d_{5/2}$ elastic lines. (d) Se/N signal ratio vs. polar angle.

3. Stoichiometry and thickness estimation

For the XPD experiments in SI Fig. 2. and the XPS experiments in SI Fig. 3., we used non-monochromatised Mg Kα radiation. For XPS a Shirley function was used to approximate the background. The data show that both $MoSe_2$ and *h*-BN are present in the XPS spectra (SI Fig. 3a). The red markers represent the experimental data, and the peak fittings in blue curves are derived from Voigt line shape approximations. The deconvoluted peaks are shown in black. The Se 3s is considered in the Mo 3d peak-window, and Mo 3p in the N 1s peak-window. The intensities were normalized by the corresponding subshell cross-sections and the nominal emitter density excluding the double Se occupancy per unit cell. As a result, the portion of the elements is B: 8±2 % , N: 8±2 %, Mo: 35±3 %, and Se: 49±5 %. While the stoichiometry of the BN film is maintained, the sample appears as a Se-deficient $MoSe_2$ layer.

In order to estimate the thickness of as-grown $MoSe_2$, we assume a uniform $MoSe_2$ coverage on top of an *h*-BN layer in the examined region. From the measured Mo$3d_{5/2}$ and B1s intensities, the photoemission cross sections and the areal emitter densities we get with a photoelectron mean free path of 20 Å and a BN layer thickness of 3.3 Å an average layer thickness of 1.8 monolayers of $MoSe_2$.

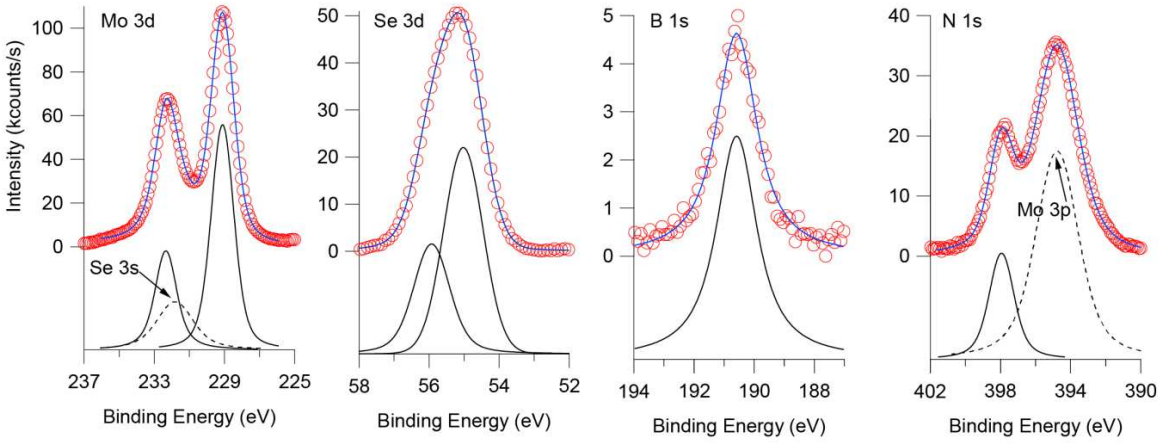

SI Fig. 3. Stoichiometry and thickness estimation. Black lines represent the deconvolution of XPS core levels.

4. Raman spectra of transferred $MoSe_2$/*h*-BN heterostructures

The Raman spectra feature the A_{1g} mode at ~ 240 cm^{-1} for both as-grown $MoSe_2$ and transferred heterostructure, where the optical image is shown in the inset. The corresponding PL is shown in the main text. The peak at ~ 520 cm^{-1} is from the SI.

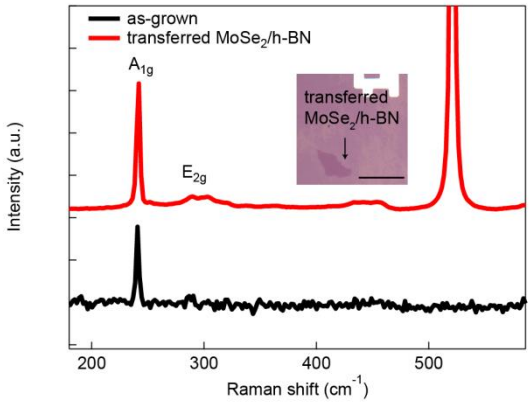

SI Fig. 4. **Raman spectra of as-grown and transferred $MoSe_2$/*h*-BN heterostructure.** The A_{1g} mode of ~ 240 cm^{-1} remains unchanged. The inset shows the optical image of the transferred heterostructure. The scale bar is 25 μm.

5. Electronic structures of submonolayer $MoSe_2$/*h*-BN/Rh(111)

We grow submonolayer $MoSe_2$ on h-BN for investigations of the surface at the initial growth stage. After a growth time of 10 min, we obtain an estimated nominal thickness of < 0.3 ML $MoSe_2$. In the *k*PEEM results, we do not observe the band dispersions from $MoSe_2$ but only from *h*-BN/Rh(111). The valence band structure of *h*-BN/Rh(111) comprises two distinct bands, σ-band and π-band that can be both observed with an excitation source He I α ($h\nu$ = 21.2 eV). At the Γ point in binding energy of 4 eV, the σ-band splits into two in the direction away from Γ point. However, at the Γ point, we do not observe the splitting of the σ-band, which is the feature of nanomesh of pristine ML *h*-BN/Rh(111) system. We suspect the decoupling takes place at early growth stages where the nanomesh structure are smeared out due to the adatom modification, resulting in the degeneracy of the σ-band at the Γ point.[1] On the other hand, the π-band disperses from the binding energy of 8.4 eV at Γ point and up to energy of 2.4 eV at the *K* point.

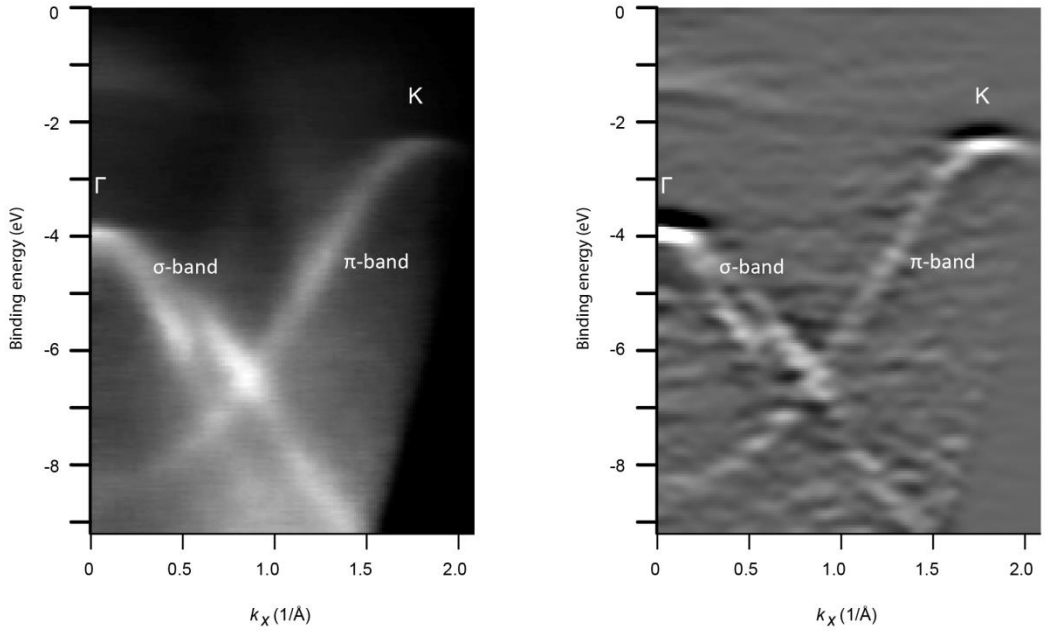

SI Fig. 5. Electronic structure of *h*-BN/Rh(111). (a) *k*-space along the *Γ* to *K* direction and (b) the second derivative band structure of *h*-BN/Rh(111).

6. Energy difference between Γ and K and the effective mass calculation

In order to differentiate the energies between *Γ* and *K*, we performed the cuts along *Γ* and *K*, and plotted the intensity profile. The analyzer pass energy of 50 eV with an entrance slit size of 1 mm provided an energy resolution of 100 meV. The energy difference can be determined by comparing the two peaks. Since the splitting of the *K* point cannot be resolved, we can only observe one broad peak for the *K* point cut, and the broadening might result in an underestimation of the energy difference. We can further derive the hole effective mass at the *K* point by fitting the band dispersion with the equation $E = \hbar^2k^2/2m^*$, where $\hbar$ is the reduced Planck constant and m^* is the effective mass. The effective mass is determined to be $m/m^* = 1.0 \pm 0.1$, and is slightly higher than the calculated value reported in literature.[3]

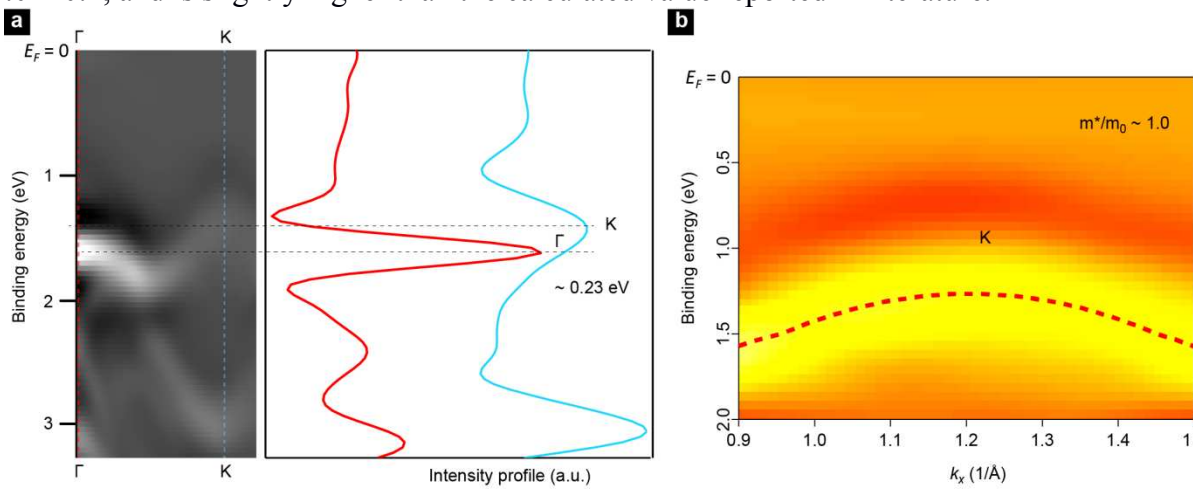

SI Fig. 6. Energy difference between *Γ* and *K* and the effective mass calculation. (a) The red and blue curves on the right panel are derived from the cuts along *Γ* and *K*, indicated by the dashed lines in the experimental band structure. (b) The hyperbolic fitting (red dashed line) of the dispersion near *K* showing the effective hole mass.

7. Electronic structures along the *Γ* to *M* direction

We plot the band structure of the ML $MoSe_2$/*h*-BN heterostructure along the *Γ* to *M* direction and compare with the calculated band structure. In spite of the high similarity between the experimental and theoretical band structures, we noticed that the topmost band dispersion at the *M* point is lifted up and deviates from the calculated curve. The up-lift might be due to the mixed signals from the misoriented $MoSe_2$ or the band compression effect discussed in the main text, but the origin is not clear and needs more investigation in the future.

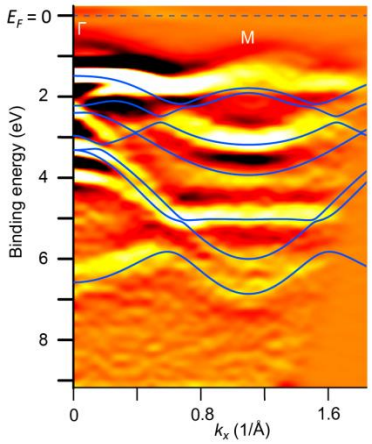

SI Fig. 7. **Electronic structure of ML $MoSe_2$/*h*-BN along the *Γ* to *M* direction.** The blue curves are the calculated band structures of freestanding ML $MoSe_2$.

8. DFT calculations of $MoSe_2$/*h*-BN heterostructures

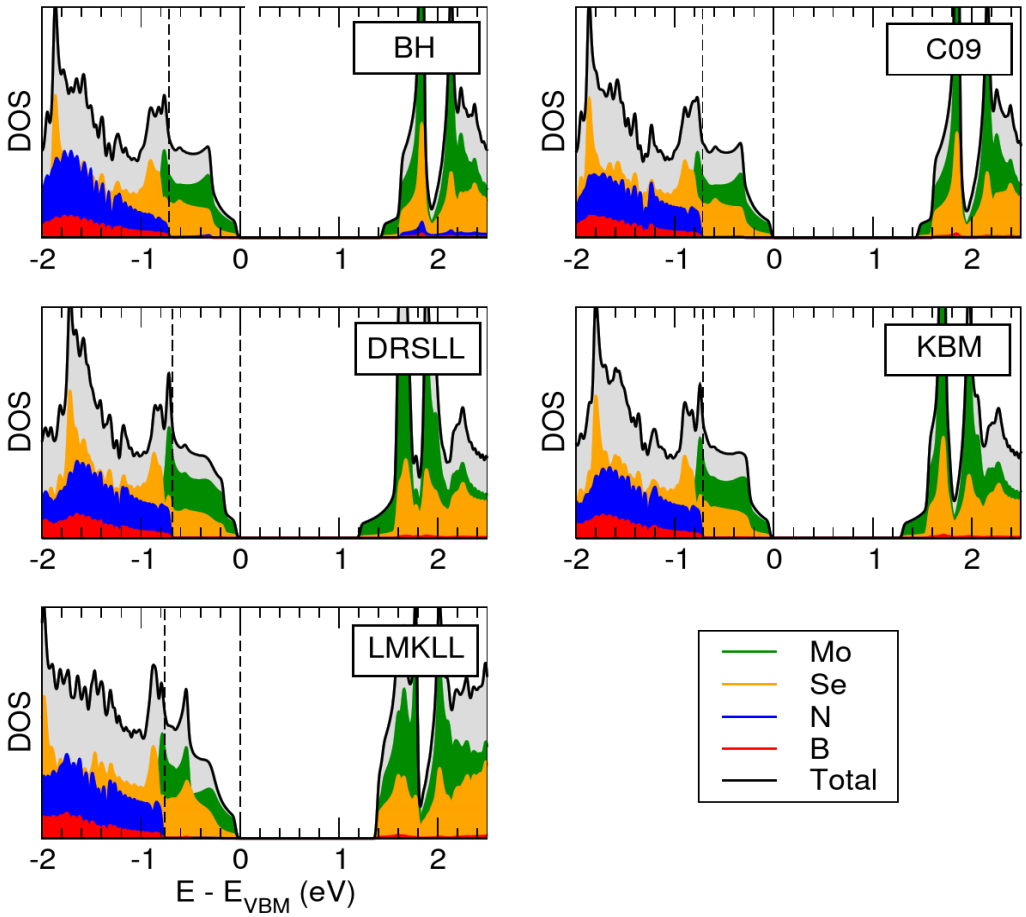

SI Fig. 8. **Electronic density of states (DOS) of $MoSe_2$/*h*-BN heterostructure from DFT calculations for different vdW functionals.** Vertical dashed lines indicate band edges of $MoSe_2$ and *h*-BN. Electronic states for B and N were doubled to help the eye. Note that *h*-BN states are located well below the $MoSe_2$ valence band maximum and do not contribute to the valence band edge.

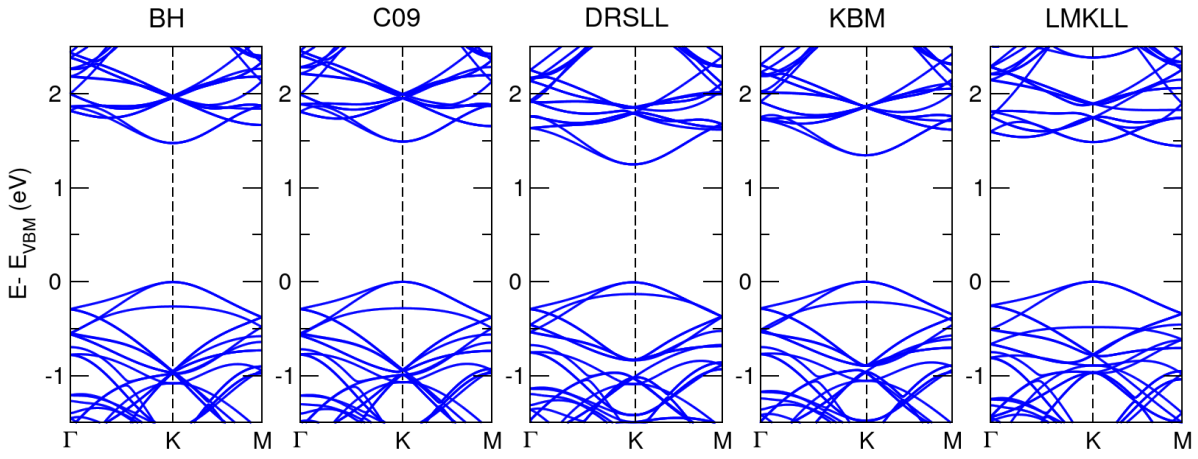

SI Fig. 9. **Electronic band structures of $MoSe_2$/*h*-BN heterostructure from DFT calculations for different vdW functionals.** Note that the direct bandgap of ML $MoSe_2$ is preserved in the heterostructure. Note that the direct band gap of ML $MoSe_2$ is preserved in the heterostructure.

Van der Waals functional	$h_{MoSe2/h\text{-}BN}$ (Å)	E_{inter} (meV / $MoSe_2$ f.u.)	$\varepsilon_{h\text{-}BN}$ (%)
BH	3.65	-85	0.48
C09	3.54	-92	0.67
DRSLL	3.74	-93	-1.5
KBM	3.66	-108	-0.87
LMKLL	3.58	-106	0.75

Supplementary Table 1. **Structure and energetics of the $MoSe_2$/*h*-BN heterostructure from DFT calculations.** Interlayer distance ($h_{MoSe2/h\text{-}BN}$), interaction energy (E_{inter}) and strain in *h*-BN ($\varepsilon_{h\text{-}BN}$) for different van der Waals functionals. Interlayer distance is defined as the average difference in height between the *h*-BN plane and the $MoSe_2$ bottom Se layer. Interaction energy is defined as the difference in total energy between the $MoSe_2$/*h*-BN heterostructure and isolated $MoSe_2$ and *h*-BN per $MoSe_2$ formula unit.

REFERENCES

(1) Roth, S.; Greber, T.; Osterwalder, J. Some Like It Flat: Decoupled h-BN Monolayer Substrates for Aligned Graphene Growth. *ACS Nano* **2016**, *10*, 11187–11195.

(2) Barja, S.; Wickenburg, S.; Liu, Z.-F.; Zhang, Y.; Ryu, H.; Ugeda, M. M.; Hussain, Z.; Shen, Z.-X.; Mo, S.-K.; Wong, E.; Salmeron, M. B.; Wang, F.; Crommie, M. F.; Ogletree, D. F.; Neaton, J. B.; Weber-Bargioni, A. Charge Density Wave Order in 1D Mirror Twin Boundaries of Single-Layer $MoSe_2$. *Nat. Phys.* **2016**, *12*, 751–756.

(3) Horzum, S.; Sahin, H.; Cahangirov, S.; Cudazzo, P.; Rubio, A.; Serin, T.; Peeters, F. M. Phonon Softening and Direct to Indirect Band Gap Crossover in Strained Single-Layer $MoSe_2$. *Phys. Rev. B* **2013**, *87*, 125415.